Programming Self-Assembly of DNA Origami Honeycomb Two-Dimensional Lattices and Plasmonic Metamaterials

Pengfei Wang,[†] Stavros Gaitanaros,[‡] Seungwoo Lee,[§] Mark Bathe,[‡] William M. Shih,[||] and Yonggang Ke*,[†]

[†]Wallance H. Coulter Department of Biomedical Engineering, Georgia Institute of Technology and Emory University, Atlanta, Georgia 30322, United States

[‡]Department of Biological Engineering, Massachusetts Institute of Technology, Cambridge, Massachusetts 02139, United States

[§]SKKU Advanced Institute of Nanotechnology & School of Chemical Engineering, Sungkyunkwan University (SKKU), Suwon, 16419, Republic of Korea

[||]Wyss Institute for Biologically Inspired Engineering and Department of Cancer Biology, Dana-Farber Cancer Institute, and Department of Biological Chemistry and Molecular Pharmacology, Harvard Medical School, Harvard University, Boston, Massachusetts 02115, United States

ⓢ *Supporting Information*

ABSTRACT: Scaffolded DNA origami has proven to be a versatile method for generating functional nanostructures with prescribed sub-100 nm shapes. Programming DNA-origami tiles to form large-scale 2D lattices that span hundreds of nanometers to the micrometer scale could provide an enabling platform for diverse applications ranging from metamaterials to surface-based biophysical assays. Toward this end, here we design a family of hexagonal DNA-origami tiles using computer-aided design and demonstrate successful self-assembly of micrometer-scale 2D honeycomb lattices and tubes by controlling their geometric and mechanical properties including their interconnecting strands. Our results offer insight into programmed self-assembly of low-defect supra-molecular DNA-origami 2D lattices and tubes. In addition, we demonstrate that these DNA-origami hexagon tiles and honeycomb lattices are versatile platforms for assembling optical metamaterials via programmable spatial arrangement of gold nanoparticles (AuNPs) into cluster and superlattice geometries.
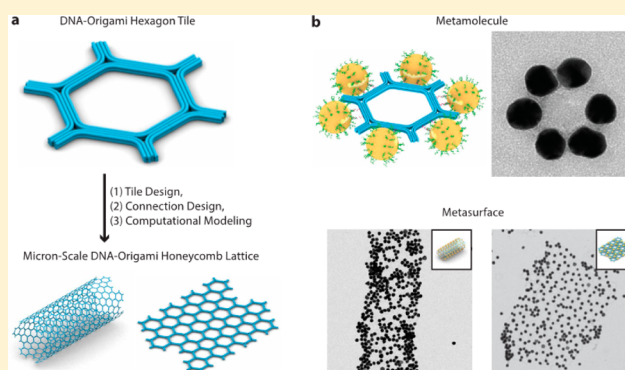
INTRODUCTION

Well-ordered one-dimensional (1D), two-dimensional (2D), and three-dimensional (3D) nanostructures, for example, carbon nanotubes, graphene, inorganic nanoparticle superlattices, and DNA crystals, are useful in applications including nanoelectronics, sensors, and nanooptics. Self-assembly of programmable nanomaterials is a promising route to building such well-ordered nanostructures due to their nanometer-scale precision, low cost, and potential for parallel and therefore scalable synthesis. An appealing class of programmable, self-assembling nanomaterial is DNA: using programmed complementarity, DNA strands self-assemble into prescribed nanostructures with nanoscale precision.[1] The field of structural DNA nanotechnology has produced many sophisticated nanostructures of variable size and complexity.[2−15] These DNA assemblies have been employed for applications such as nanomedicine,[16−22] nanoplasmonics,[23,24] nanoelectronics,[3,25] and inorganic nanoparticle synthesis.[26]

The scaffolded DNA-origami approach[4] offered a major advance in increasing the complexity of DNA nanostructures that can be self-assembled. This powerful strategy is capable of synthesizing discrete, fully addressable nanostructures. Researchers have also grown sub-100 nm DNA origami into hierarchically assembled 1D, 2D, and 3D periodic structures at the micrometer-scale: several successful examples have utilized sticky-ended cohesion,[14,27−31] blunt-ended interactions,[32] and substrate-assisted self-assembly.[33−36] However, a robust design strategy for programmed self-assembly of ordered 2D DNA-origami lattices remains to be achieved. In addition, elucidating the design factors that reduce disordered aggregates and favor the formation of flat lattices or curved tubes remains an important challenge. In contrast, lower molecular weight, multistranded DNA tiles have been investigated in greater detail for their ability to self-assemble into tubes[37−43] versus lattices.[2,3,44−50]

Here we report a family of DNA-origami hexagon tiles (HT) that can be programmed to assemble into honeycomb lattices that form either tubes or flat 2D planar lattices (Figure 1). Our approach combines rational design with feedback from
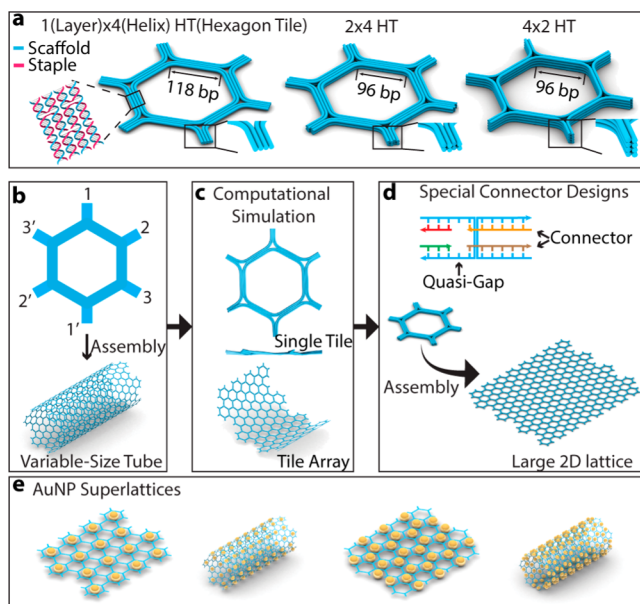
Figure 1. Programming self-assembly of DNA-origami honeycomb lattices. (a) Schematics of DNA-origami hexagon tiles of the 1 × 4 HT, 2 × 4 HT, and 4 × 2 HT. Each cylinder represents a DNA duplex. The insets show detailed information on the connection arms. The side length of each HT in terms of base pairs (bp) is indicated. (b) Self-assembly of DNA-origami tubes. (c) Computational simulation to model the mechanical properties of individual tiles and tile array curvatures. d) Connector designs to tune array curvature to facilitate the formation of 2D lattices. (e) Microscale AuNP superlattices fabricated from DNA-origami 2D lattices or tubes.

computational modeling to control the mechanical properties of individual DNA-origami tiles, as well as interconnections between individual tiles. We also demonstrate that the as-assembled HTs and lattices could be utilized for constructing plasmonic metamaterials via deterministic arrangement of gold nanoparticles (AuNPs).

DESIGN

Our design strategy utilizes a DNA-origami HT with six protruding arms that can be connected to six identical neighboring tiles to produce lattice structures. Self-assembly of HTs can lead to the formation of either tubes or 2D lattices. Three types of HT were designed for the study (Figure 1a): a single-layer, four-helix HT (1 × 4 HT, 4248 bp, Figure S3), a double-layer, eight-helix HT (2 × 4 HT, 6912 bp, Figure S4), and a quadruple-layer, eight-helix HT (4 × 2 HT, 6912 bp, Figure S5). Each HT incorporates a single M13-based scaffold per hexagon and displays 6-fold rotational pseudosymmetry (i.e., sequence is different for each arm). Structurally, a HT can be considered as consisting of six three-point-star units of equal size, where we implemented a "curved helix" design at each junction to achieve three-point-star units. This curved helix design may provide greater structural rigidity in comparison with connecting arms using single-stranded linkages (refer to Figure S2 for additional information and discussion). These three HT designs enabled us to systematically test how tile rigidity impacts both individual tiles and their differential self-assembly into tubes versus 2D lattices. In addition, we utilized computational modeling to gain insight into mechanisms by which the tiles' mechanical properties and their highly nonlinear interactions impact the large-scale assemblies (Figure

1c). Finally, we systematically examined a variety of intertile connection strand schemes (Figure 1d, Figure S8). Our results suggest that accumulation of out-of-plane curvature during HT self-assembly can be tuned by connector design, ultimately resulting in control over the formation of either tubes or 2D lattices on the micrometer scale (Figure 1b,d). In addition, we demonstrate a gold nanoparticle (AuNP) cluster organized on DNA-origami tile behaving as a plasmonic metamolecule with a magnetic dipolar resonance mode and a hexagonally arranged AuNP monolayer lattice, organized by an underlying DNA-origami lattice, behaving as a plasmonic metasurface with controlled electric resonances (Figure 1e).

TUBES ASSEMBLED FROM DNA-ORIGAMI HEXAGON TILES

We first characterized the formation of HT monomers. For each HT, a strong single band with lower mobility than the scaffold band was observed on native agarose gels (Figure 2a–
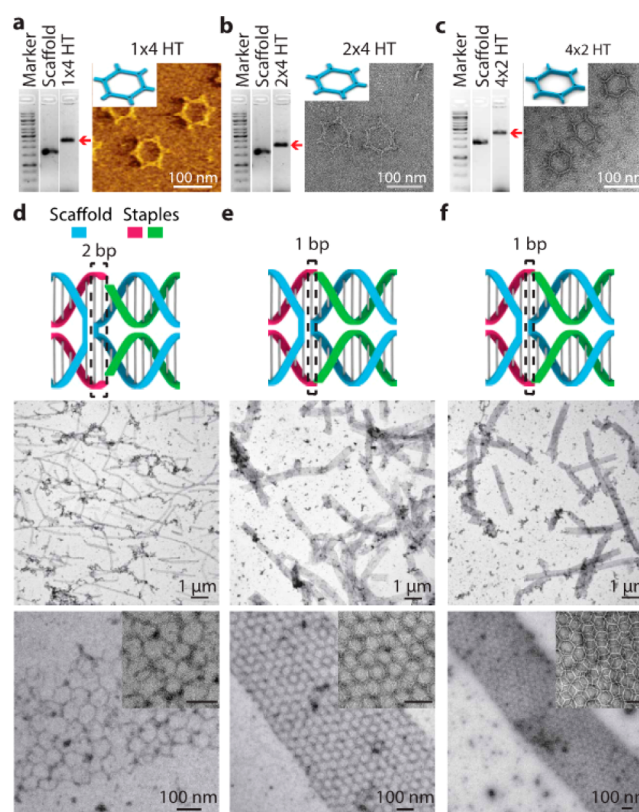

Figure 2. Assembly of DNA-origami HTs and tubes. (a−c) Agarose gel electrophoresis and AFM/TEM confirm the formation of the 1 × 4 HT, 2 × 4 HT, and 4 × 2 HT, respectively, without connector strands. (d−f) Tubes assembled from the 1 × 4 HT, 2 × 4 HT, and 4 × 2 HT, respectively, using either 2-bp or 1-bp connectors, as illustrated on top of the TEM images. Zoom-in images are shown as insets to illustrate the detailed overlapped hexagonal patterns of tubes. Scale bars: 100 nm.

c). Gel-purified samples showed nanostructures with expected morphologies matching with designed objects in AFM images and TEM images. Assembly of periodic nanostructures was realized by connecting neighboring HTs using a total of 8 base-pair (bp) sticky-end connections per arm. For the 1 × 4 HT, each connector strand contained a 2-bp sticky end. In contrast, each connector strand for the 2 × 4 HT or the 4 × 2 HT

Table 1. Statistics of HT Assembly

hexagon tile	connector	morphology	tube width (μm)	maximum length of tube (μm)	maximum size of 2D lattice (μm^2)
1 × 4 HT	2-bp	narrow tube	0.26 ± 0.05	15.0	a
4 × 2 HT	2-bp	tube	0.72 ± 0.09	5.5	a
	1-bp	tube	0.69 ± 0.05	10.1	a
	l-bp-quasi-gap	tube	0.89 ± 0.07	6.8	a
2 × 4 HT	2-bp	mostly aggregate	a	a	0.4 × 0.6
	2-bp-quasi-gap	tube	0.95 ± 0.14	8.1	a
	2-bp-gap	tube	1.12 ± 0.04	6.5	a
	1-bp	tube	0.82 ± 0.13	13.6	a
	1-bp-quasi-gap	large 2D lattice	a	a	6 × 9
	1-bp-gap	2D lattice	a	a	1.5 × 4
	blunt end	2D lattice	a	a	1.5 × 2
	2-nt loop	small 2D lattice	a	a	0.5 × 0.8

^{a}Not applicable.
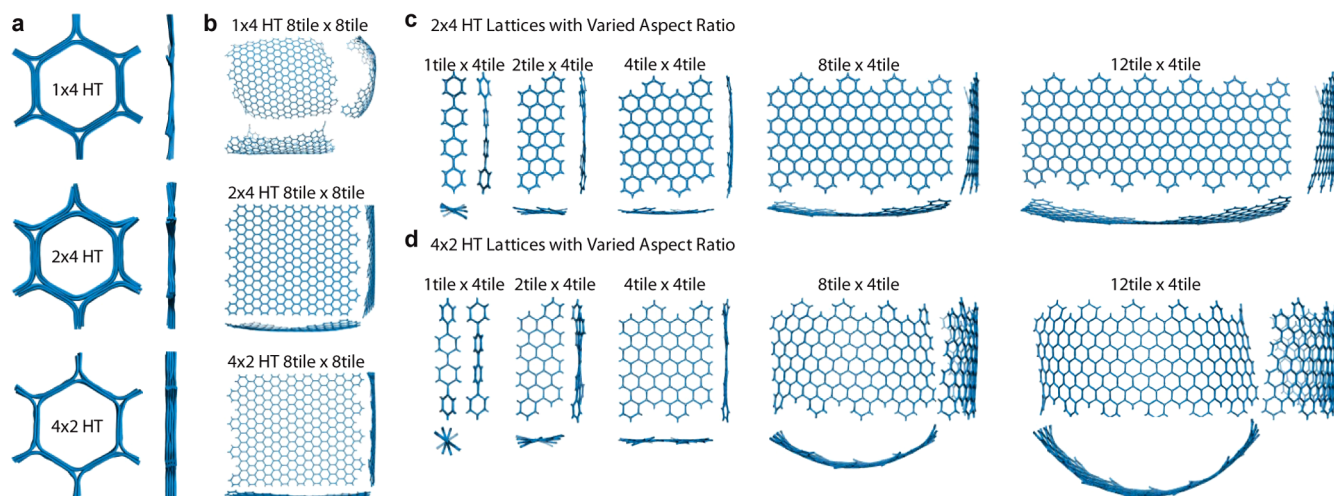

Figure 3. Structure modeling of DNA-origami HTs and lattices. (a) Solution shapes of the 1 × 4 HT, 2 × 4 HT, and 4 × 2 HT. (b) Simulated lattices of the 1 × 4 HT, 2 × 4 HT, and 4 × 2 HT composed of 8 tiles × 8 tiles. (c) Simulated 2 × 4 HT lattices with varied aspect ratio. (d) Simulated 4 × 2 HT lattices with varied aspect ratio.

contained a 1-bp sticky end. TEM images showed that all three HTs formed micrometer-length tubes (Figure 2d−f), with length ranging from several micrometers to greater than 10 μm. Closer inspection of the 1 × 4 HT tube revealed that many 1 × 4 HTs exhibited noticeable deformation (Figure 2d, Figure S11), likely due to the low rigidity of their single-layer design that rendered them susceptible to strain induced by the deposition or staining process. In comparison, the 2 × 4 HT (Figure 2e, Figure S15) and 4 × 2 HT (Figure 2f, Figure S21) tubes maintained intact hexagonal morphology due to their enhanced tile rigidity. The mean width of the tubes for the 1 × 4 HT, the 2 × 4 HT, and the 4 × 2 HT were 0.26 ± 0.05, 0.82 ± 0.13, and 0.69 ± 0.05 μm, respectively (Table 1). The considerably narrower width of the 1 × 4 HT tubes may be due to the relatively lower area moment of inertia (i.e., ability to resist bending) of the single-layer tile, which may lead to greater intratile curvature. This is in contrast with the 2 × 4 and 4 × 2 HTs that have higher bending rigidity and self-assembled into larger diameter tubes. Somewhat surprisingly, however, the 2 × 4 HT tubes were of considerably greater diameter than the 4 × 2 HT tubes, even though the latter consists of quadruple layers, which we expect to exhibit greater resistance to out-of-plane bending.

LATTICE STRUCTURE MODELING

Numerical simulations were performed using the computational framework CanDo[51−53] in order to investigate potential geometric and mechanical origins for tube formation to be favored over 2D lattice formation and to probe the structural origin for the formation of larger diameter tubes by the 2 × 4 HT. Simulated solution shapes of individual tiles (Figure 3a) showed minimal intrinsic bending for each individual HT; in contrast, all three HT designs showed significant intrinsic twisting, which is particularly evident when examining their protruding arms, with the 1 × 4 HT exhibiting more twisting than the 2 × 4 HT and the 4 × 2 HT. Twisting of the tiles may be attributed to underwinding of the DNA helices: 10.67 bp/turn in the current square-lattice designs compared with the natural helicity of B-form DNA, which is 10.5 bp/turn. This intrinsic twist of the individual HT is expected to impact the overall solution shape of their self-assembled lattices since it introduces a geometric mismatch into tile interconnections. Normal mode analysis (NMA) revealed that the 1 × 4 HT is significantly more compliant than the other two HT designs, while the 2 × 4 HT appears to be the least compliant due to its greatest cross-section or second moment of area (Figure S9). Prediction of the equilibrium solution shapes of isotropic lattices consisting of 8 × 8 tiles (Figure 3b) revealed significant
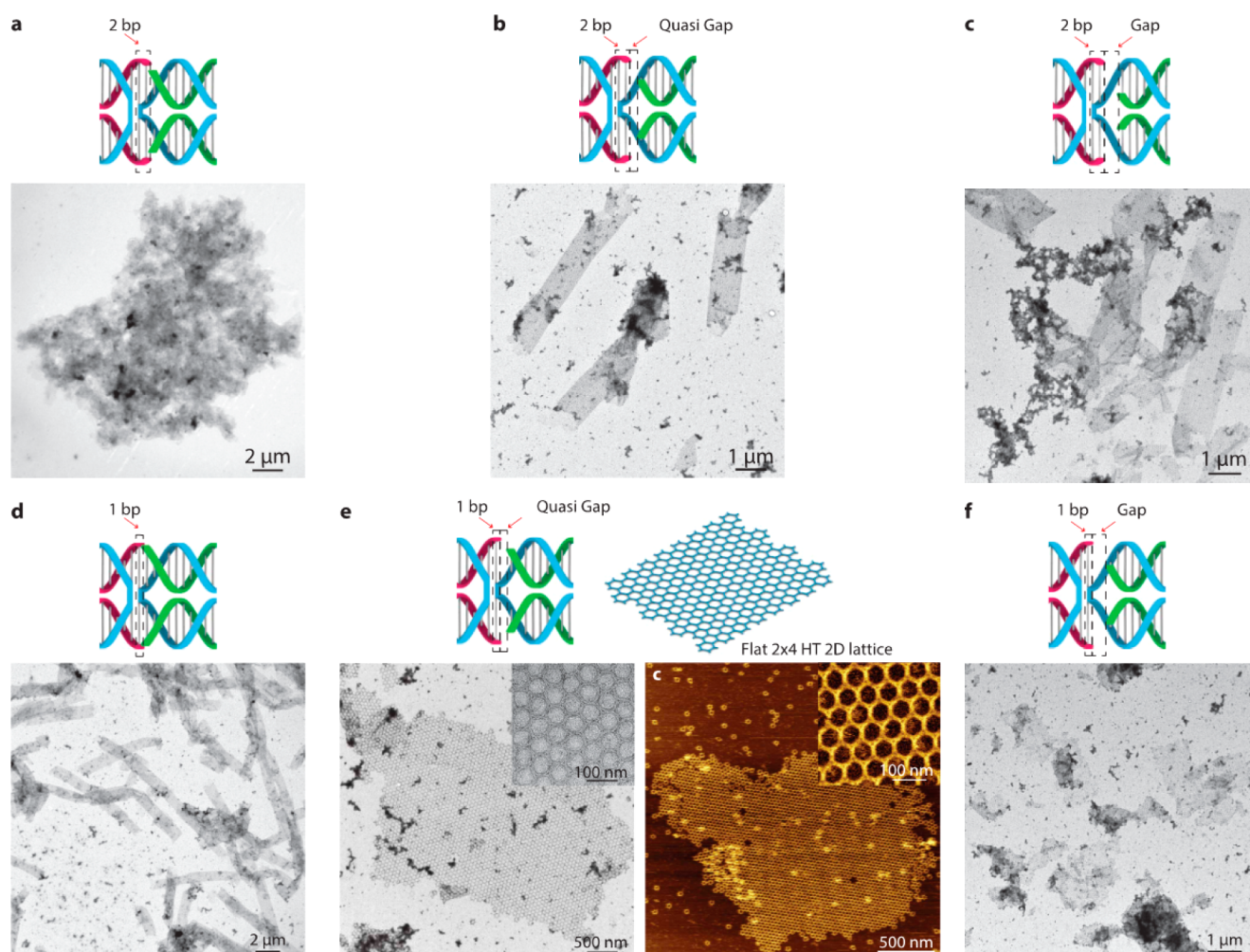
Figure 4. Tuning curvature of the 2 × 4 HT assembly via connector designs. (a) Aggregates of small lattices assembled from the 2 × 4 HT using 2-bp connectors. (b) Tubes assembled from the 2 × 4 HT using 2-bp-quasi-gap connectors. (c) A mixture of tubes and 2D lattices assembled from the 2 × 4 HT using 2-bp-gap connectors. (d) Tubes assembled from the 2 × 4 HT using 1-bp connectors. (e) Large 2D lattices assembled from the 2 × 4 HT using 1-bp-quasi-gap connectors: (left) TEM image; (right) AFM image. Inset images are present to show detailed pattern of 2D lattice. (f) Small 2D lattices assembled from the 2 × 4 HT using 1-bp-gap connectors.

bending and twisting of lattices composed of the 1 × 4 HT, whereas the other two HTs, which have bending and twisting stiffnesses considerably greater than those of the 1 × 4 HT, appeared relatively flat. Differences between the 2 × 4 HT and the 4 × 2 HT were more nuanced since contrasting patterns emerged when the aspect ratios of these lattices was varied. For example, simulations of lattices of high aspect ratio exhibited significant out-of-plane distortions for the 4 × 2 HT (Figure 3d), whereas the corresponding solution shapes of the 2 × 4 HT were largely insensitive to aspect ratio (Figure 3c, Figure S10). We attribute this feature to the geometric mismatch caused by the intrinsic twist of each tile. This mismatch appeared to be significantly more pronounced in the 4 × 2 HT than in the 2 × 4 HT, as is evident from Figure 3d, which shows that the 1 tile ×4 tile lattice is highly twisted. The twist of the 4 × 2 HT produced a rotation that is nearly twice that of the corresponding one of the 2 × 4 HT. In an isotropic lattice, however, this angle of twist is constrained by the increased number of interconnecting arms, as revealed in the 4 tile ×4 tile lattice of the 4 × 2 HT. While the exact mechanism for the global deformations of the larger rectangular lattices of the 4 × 2 HT is unclear, they may be due to mechanical instabilities

caused by accumulation of in-plane strain energy produced by suppressing the intrinsic twist of the tile. In summary, among the three HTs investigated using computational modeling, the 2 × 4 HT was found to be the most robust design in terms of remaining flat despite variations in size and aspect ratio of the lattice.

TUNING LATTICE CURVATURE VIA CONNECTORS

The preceding simulation results revealed significant twisting of the protruding arms of the HTs, which, we hypothesized, may be a principal contributor to the accumulation of intertile curvature. Therefore, we systematically designed and tested different connector strand designs to study how these designs would affect lattice curvature. The 2 × 4 HT was chosen for this study because of its lower degree of curvature accumulation, as demonstrated by experiment and corroborated by simulation. First, we altered intertile binding strength by employing connector strands that contained 2-bp, 1-bp, or 0-bp ("blunt end") sticky-ends. Second, we introduced one ("quasi-gap") or two ("gap") unpaired scaffold bases between each pair of connected DNA duplexes at the interarm connection domains. Overall, a total of eight connector designs were
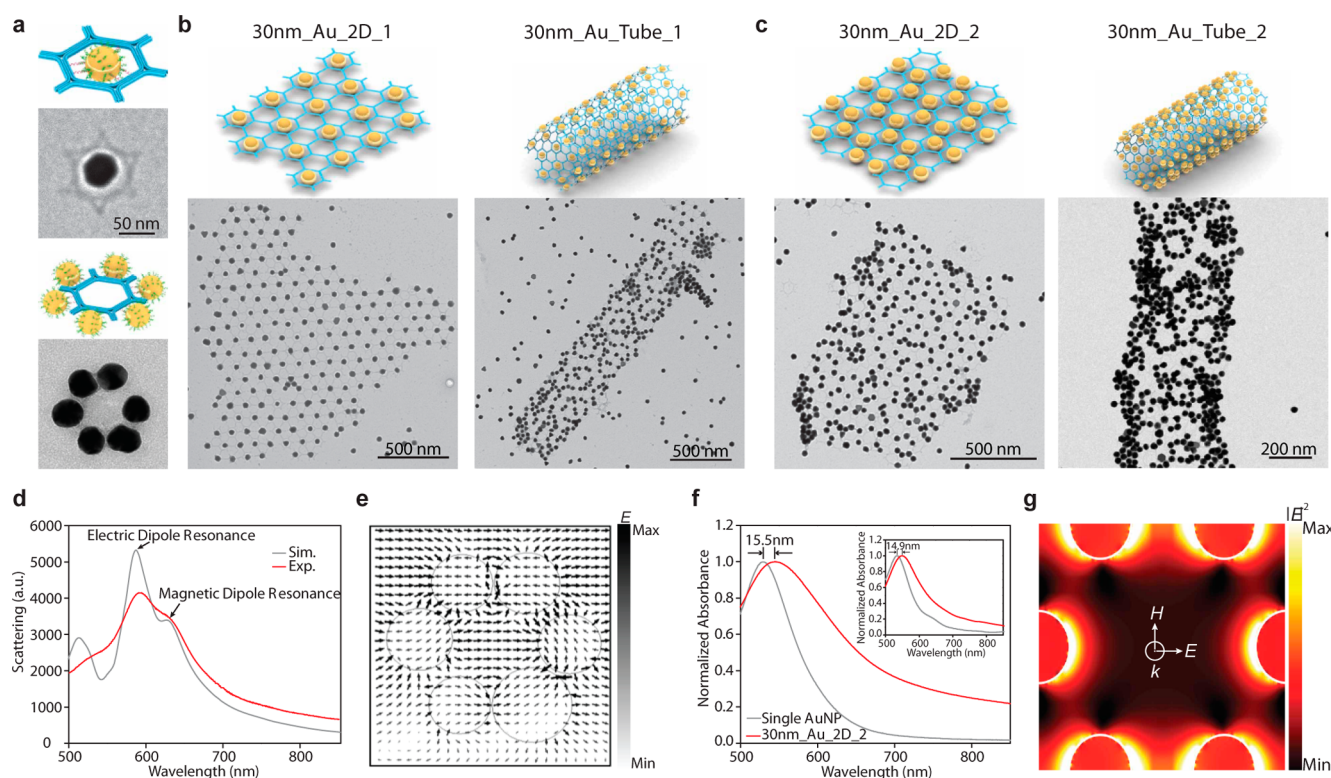
Figure 5. Plasmonic metamaterials assembled on the 2 × 4 HT: (a) 30 nm AuNP monomer (top) and hexamer (bottom) assembled on a hexagon tile; (b) 30 nm AuNP superlattices assembled on hexagonal 2D lattices and tubes occupying type-1 cavity; (c) 30 nm AuNP superlattices assembled on hexagonal 2D lattices and tubes occupying type-2 cavity; (d) simulated and experimental dark-field scattering spectra of the 30 nm AuNP hexamer structure; (e) spatial distribution of electric field displacement (E) at the wavelength of magnetic response of the 30 nm AuNP hexamer structure; (f) Experimental and simulated (inset figure) UV−vis absorption spectra of single 30 nm AuNP and 30nm_Au_2D_2 superlattice; experimental measurement reveals a 15.5 nm red-shift of the 30nm_Au_2D_2 superlattice compared with a single 30 nm AuNP, which matches well with simulated result of a 14.9 nm red-shift; (g) electric field intensity ($|E|^2$) distribution within a unit of the 30nm_Au_2D_2 superlattice. The spatial distribution of coupled electric field intensity is well revealed between AuNPs.

tested on the 2 × 4 HT: 2-bp, 2-bp-quasi-gap, 2-bp-gap, 1-bp, 1-bp-quasi-gap, 1-bp-gap, blunt end, and 2-nt loop (Figure S8). We speculate that the quasi-gap or gap design may play similar roles as deleting bases between crossovers to address the underwinding of DNA helixes. Alternatively, increased flexibility in the quasi-gap and gap designs may alleviate strain accumulation in the DNA-origami assembly and thereby favor the relative formation of 2D lattice versus tube.

We observed that 2-bp connectors yielded mostly aggregates of small lattices: the strong connections in this design may promote irreversible assembly and therefore lock in defects, thereby leading to aggregation (Figure 4a, Figure S12). Tubes were observed when 2-bp-quasi-gap connectors were used (Figure 4b, Figure S13). Wider tubes and unclosed structures were found if 2-bp-gap connectors were used (Figure 4c, Figure S14). The formation of wider tubes with use of 2-bp-gap connectors confirmed that implementation of an unpaired scaffold base at the connection domains could indeed help mitigate curvature accumulation during assembly. Since the curvature was not sufficiently reduced by 2-bp-gap connectors to favor the formation of flat 2D lattice, a mixture of closed and unclosed structures was observed. We then decreased the binding strength to 1-bp to promote near-reversible assembly, which, we hypothesized, would allow better healing of defects and therefore result in less aggregation. As noted earlier, tubes were formed when 1-bp connectors were used (Figure 4d). When 1-bp-quasi-gap or 1-bp-gap connector strands were used, large 2D lattices were successfully assembled (Figure 4e,f;

Figures S16 and S17). For 1-bp-quasi-gap connectors, the 2D lattices had an average size of 3 × 5 μm^2, with the largest observed 2D lattice having dimensions of 6 × 9 μm^2. Two-dimensional lattices with relatively smaller size were observed for 1-bp-gap connectors compared with 2D lattices produced from 1-bp-quasi-gap connectors. We tried to further reduce the binding strength for assembly of the 2 × 4 HT using a blunt-end connector strand design (Figure S18) and a 2-nt free-scaffold-loop design (Figure S19). For the blunt end connector design, the 2 × 4 HT could still assemble into 2D lattices of smaller dimensions, solely relying on base-pair stacking between tiles. The smaller size of the 2D lattice may be attributed to the relatively weak interactions. The 2-nt loop connector design also produced small 2D lattices with sizes up to only 200 nm, indicating that base-pair stacking between tiles was not fully shielded by the 2-nt loop.

Using the same 1-bp-quasi-gap connectors, the 4 × 2 HT formed tubes with relatively larger width than tubes formed from 1-bp connectors (Figure S22, Table 1), suggesting that 1-bp-quasi-gap connectors could also mitigate curvature accumulation in the assembly process of the 4 × 2 HT. However, the 4 × 2 HT assembly still favored tube formation, likely because its relatively higher tendency of curvature accumulation (in contrast to 2 × 4 HT assembly) could not be reduced to a level that favors flat 2D lattices. We then tried to design a 16-helix, quadruple-layer 4 × 4 HT to achieve higher rigidity at both out-of-plane and in-plane directions. Due to limited length of the M13 scaffold, we tested two design strategies: (1) a small

4 × 4 HT using a single DNA scaffold (Figure S6) and (2) a large 4 × 4 HT as a homohexamer that formed by six 4 × 4H-3PS DNA-origami tiles (Figure S7). Both designs showed low yields of hexagon-shaped tiles (Figures S23−25). A two-step assembly protocol using the 4 × 4H-3PS tile yielded small 2D lattices of 0.5 × 1 μm^2 (Figure S25). However, low concentration of tiles after gel purification and impurity (e.g., pentamers) may prevent assembly of larger lattices using 4 × 4H-3PS tile.

ASSEMBLY OF PLASMONIC METAMATERIALS ON ORIGAMI LATTICES

Arranging AuNPs with well-controlled pattern is of particular interest for diverse plasmonic and optical metamaterial applications.[54−63] Herein, utilizing the 2 × 4 HT DNA-origami tile and lattices, AuNP clusters and superlattices with programmed patterns were constructed by anchoring AuNPs within the tile plane through single-stranded capture strands that protruded out from the HT (Figure S26). AuNP monomer and hexamer were assembled on the HT monomer by integration of 30 nm AuNPs at the interior or exterior sides of hexagon (Figure 5a). Both native agarose gel electrophoresis and TEM imaging confirmed the successful construction of AuNP monomer and hexamer with yield of targeted patterns of 92% and 70%, respectively (Figure S27). Micrometer-area superlattices of AuNPs were fabricated on DNA-origami 2D lattices and tubes via capturing AuNPs within either the intratile hexagon cavity (type-1 cavity) or the intertile hexagon cavity (type-2 cavity). Two types of AuNP superlattice patterns were designed and fabricated (Figure 5b,c): (1) 30 nm AuNPs occupying type-1 cavities in 2D lattices (30nm_Au_2D_1) and tubes (30 nm_Au_tube_1); (2) 30 nm AuNPs occupying type-2 cavities in 2D lattices (30nm_Au_2D_2) and tubes (30 nm_Au_tube_2). TEM imaging revealed the successful construction of AuNP superlattices. More TEM images of AuNP superlattices are included in Figures S28−S31.

The AuNP hexamer and lattices exhibited interesting plasmonic resonance both in simulation and in experiment (Figure 5d−g, Figure S32). The numerical calculation (powered by finite-difference, time-domain (FDTD)) of scattering spectra of the 30 nm AuNP hexamer in Figure 5a showed the magnetic dipolar resonance mode (scattering peak at 645 nm) together with fundamental electric resonance mode (scattering peak at 587 nm) for this AuNP cluster (Figure 5d; gray line). The simulation results were confirmed by dark-field scattering measurements (Figure 5d; red line). This artificial optical magnetism of the AuNP cluster can be further evidenced by the circularly rotating electric displacement (black arrow in Figure 5e) at the wavelength of 645 nm. The 30nm_Au_2D_2 lattices (Figure 5f) displayed the characteristics of electrical optical metamaterials resulting from enhanced interparticle coupling. We observed a 15.5 nm red-shift on the UV−vis absorption spectra compared with discrete 37 nm AuNPs (Figure 5f). This shift is in good agreement with the 14.9 nm red-shift obtained from simulation done on 37 nm AuNP lattice with 20 nm interparticle distance. Both AuNP diameter and interparticle distance were determined from TEM measurements. This capacitive coupling-enabled electric resonance within the AuNP superlattice was further confirmed by the spatial distributions of coupled electric field intensity between AuNPs (Figure 5g). Thus, our DNA-origami HT and lattice provide a versatile platform for the nanoengineering of artificial plasmonic metamolecules and metasurfaces.

CONCLUSION

In summary, we have successfully constructed micrometer-scale DNA-origami tubes from 1 × 4 HT, 2 × 4 HT, and 4 × 2 HT, and 2D lattice from 2 × 4 HT. The DNA-origami lattice structures realized in current study are relatively easy to produce, in comparison with previous lattices: the HT lattices were prepared in solution without substrate assistance[33−36] in a facile one-pot assembly without purification of origami tiles[27] or careful adjustment of thermal annealing protocol.[27−30] We showed a robust design paradigm for producing micrometer-scale DNA-origami lattice structures. Our method combines rationally designed origami tiles with tunable mechanical properties, computational simulation of tiles and lattices, and systematic variation of intertile connections. From experimental observation and computational simulation, we found that several factors may play important roles in determining the assembly results of DNA-origami HTs: (1) intrinsic out-of-plane tile bending; (2) out-of-plane flexural rigidity; (3) intrinsic twisting of the tile; and (4) connector strand design. Intrinsic tile bending or twisting could favor the accumulation of out-of-plane curvature and thus formation of tubes. In the case of minimal intrinsic tile bending or twisting, high tile rigidity generally has better resistance to out-of-plane curvature accumulation. But when tiles are designed with more rigidity to counter curvature accumulation, the best strategy may not be focusing only on increasing z-direction rigidity without considering intrinsic curvature. Both our experimental and computational studies of the 2 × 4 HT versus the 4 × 2 HT revealed that the former design yields less curvature accumulation during assembly, despite the greater rigidity along the z-direction of the 4 × 2 HT. Connector strand design is another key factor affecting accumulation of out-of-plane curvature. Extra connector binding reduces the free energy when a lattice is closed to form a tube. Therefore, stronger sticky-ends are generally considered to favor tube formation. This may explain why 2 × 4 HT assembly has a greater likelihood to form 2D lattices when 1-bp connectors are used instead of 2-bp connectors. The introduction of unpaired scaffold base into the connector strands may reduce binding strength at the connection domains due to removal of partial base-pair stacking. In addition, the unpaired scaffold base may help mitigate twisting-caused curvature accumulation. Thus, in general, introduction of an unpaired scaffold base may alleviate accumulation of curvature and facilitate the formation of wider tubes or flat 2D lattices. These observations may serve as general guidelines for future studies on the hierarchical assembly of DNA-origami tiles. Kinetic modeling of tile-assembly dynamics in the future may offer a more comprehensive picture and clearer guidelines for controlling the assembly outcome of DNA-origami tiles.

Honeycomb DNA-origami lattices are useful template structures for many potential applications, such as metamaterial fabrication via spatial arrangement of functional nanomaterials or nanolithography fabrication being utilized as lithography masks. As a demonstration, herein, we implemented such rationally designed DNA-origami motifs into the assembly of plasmonic metamaterials. The advance in the deterministic arrangement of noble metallic NPs can reshape currently available engineering of unnatural light−matter interaction at the optical domain.[54−57] In line with this, our DNA-origami designs (HT and HT lattice) have the capability to expand the design space of accessible AuNP optical metamaterials through

exquisite control over geometry and dimension. For example, the HT has been proven in this study as a versatile template to arrange AuNPs in ring geometry, so as to allow massive production of plasmonic metamolecules with artificial optical magnetism. In addition to this magnetic metamolecule, the large-area spatial arrangement of AuNPs into superlattices is also achieved here using HT lattices, resulting in electric metasurfaces exhibiting significant interparticle plasmonic coupling. These AuNP superlattices with a small gap, as theoretically demonstrated, allow the incoming light to be squeezed between AuNPs through capacitive coupling; thus, available epsilon and the resultant refractive index can be enhanced beyond the naturally accessible range.[55,58] Even if the currently accessible strength of such electric resonance is relatively low due to the limited coupling between AuNPs, the dispersion of the AuNP superlattice into medium (e.g., water) forming metafluids[64,65] could still expand the range of possible epsilon (Figure S33). Although not shown in the current work, the 3D tubular arrangement of AuNPs could be applicable to optical cloaking as well.[66] As such, our DNA-origami design can prove to be a versatile platform toward realization and application of AuNP based metamaterials.

■ ASSOCIATED CONTENT

Ⓢ Supporting Information

The Supporting Information is available free of charge on the ACS Publications website at DOI: 10.1021/jacs.6b03966.

> Summary figure, methods and materials, unsuccessful star motif designs, strand diagrams of hexagonal tiles and connection designs, structure modeling of hexagonal tiles and lattices, TEM images of tubes and 2D lattices, AuNP clusters and superlattices (PDF)
> Sequences of the p7560 scaffold, staples, and thiolated DNA strands (PDF)

■ AUTHOR INFORMATION

Corresponding Author

*yonggang.ke@emory.edu

Notes

The authors declare no competing financial interest.

■ REFERENCES

(1) Seeman, N. C. *Nature* **2003**, *421*, 427.
(2) Winfree, E.; Liu, F. R.; Wenzler, L. A.; Seeman, N. C. *Nature* **1998**, *394*, 539.
(3) Yan, H.; Park, S. H.; Finkelstein, G.; Reif, J. H.; LaBean, T. H. *Science* **2003**, *301*, 1882.
(4) Rothemund, P. W. K. *Nature* **2006**, *440*, 297.
(5) He, Y.; Ye, T.; Su, M.; Zhang, C.; Ribbe, A. E.; Jiang, W.; Mao, C. D. *Nature* **2008**, *452*, 198.
(6) Dietz, H.; Douglas, S. M.; Shih, W. M. *Science* **2009**, *325*, 725.
(7) Douglas, S. M.; Dietz, H.; Liedl, T.; Hogberg, B.; Graf, F.; Shih, W. M. *Nature* **2009**, *459*, 1154.
(8) Zheng, J. P.; Birktoft, J. J.; Chen, Y.; Wang, T.; Sha, R. J.; Constantinou, P. E.; Ginell, S. L.; Mao, C. D.; Seeman, N. C. *Nature* **2009**, *461*, 74.
(9) Han, D. R.; Pal, S.; Nangreave, J.; Deng, Z. T.; Liu, Y.; Yan, H. *Science* **2011**, *332*, 342.
(10) Ke, Y. G.; Ong, L. L.; Shih, W. M.; Yin, P. *Science* **2012**, *338*, 1177.
(11) Wei, B.; Dai, M. J.; Yin, P. *Nature* **2012**, *485*, 623.
(12) Han, D. R.; Pal, S.; Yang, Y.; Jiang, S. X.; Nangreave, J.; Liu, Y.; Yan, H. *Science* **2013**, *339*, 1412.
(13) Benson, E.; Mohammed, A.; Gardell, J.; Masich, S.; Czeizler, E.; Orponen, P.; Hogberg, B. *Nature* **2015**, *523*, 441.
(14) Zhang, F.; Jiang, S.; Wu, S.; Li, Y.; Mao, C.; Liu, Y.; Yan, H. *Nat. Nanotechnol.* **2015**, *10*, 779.
(15) Veneziano, R.; Ratanalert, S.; Zhang, K.; Zhang, F.; Yan, H.; Chiu, W.; Bathe, M. *Science* **2016**, DOI: 10.1126/science.aaf4388.
(16) Ko, S. H.; Liu, H. P.; Chen, Y.; Mao, C. D. *Biomacromolecules* **2008**, *9*, 3039.
(17) Li, J.; Pei, H.; Zhu, B.; Liang, L.; Wei, M.; He, Y.; Chen, N.; Li, D.; Huang, Q.; Fan, C. H. *ACS Nano* **2011**, *5*, 8783.
(18) Walsh, A. S.; Yin, H. F.; Erben, C. M.; Wood, M. J. A.; Turberfield, A. J. *ACS Nano* **2011**, *5*, 5427.
(19) Douglas, S. M.; Bachelet, I.; Church, G. M. *Science* **2012**, *335*, 831.
(20) Jiang, Q.; Song, C.; Nangreave, J.; Liu, X. W.; Lin, L.; Qiu, D. L.; Wang, Z. G.; Zou, G. Z.; Liang, X. J.; Yan, H.; Ding, B. Q. *J. Am. Chem. Soc.* **2012**, *134*, 13396.
(21) Lee, H.; Lytton-Jean, A. K. R.; Chen, Y.; Love, K. T.; Park, A. I.; Karagiannis, E. D.; Sehgal, A.; Querbes, W.; Zurenko, C. S.; Jayaraman, M.; Peng, C. G.; Charisse, K.; Borodovsky, A.; Manoharan, M.; Donahoe, J. S.; Truelove, J.; Nahrendorf, M.; Langer, R.; Anderson, D. G. *Nat. Nanotechnol.* **2012**, *7*, 389.
(22) Zhao, Y. X.; Shaw, A.; Zeng, X. H.; Benson, E.; Nystrom, A. M.; Hogberg, B. *ACS Nano* **2012**, *6*, 8684.
(23) Kuzyk, A.; Schreiber, R.; Fan, Z. Y.; Pardatscher, G.; Roller, E. M.; Hogele, A.; Simmel, F. C.; Govorov, A. O.; Liedl, T. *Nature* **2012**, *483*, 311.
(24) Kuzyk, A.; Schreiber, R.; Zhang, H.; Govorov, A. O.; Liedl, T.; Liu, N. *Nat. Mater.* **2014**, *13*, 862.
(25) Liu, J. F.; Geng, Y. L.; Pound, E.; Gyawali, S.; Ashton, J. R.; Hickey, J.; Woolley, A. T.; Harb, J. N. *ACS Nano* **2011**, *5*, 2240.
(26) Sun, W.; Boulais, E.; Hakobyan, Y.; Wang, W. L.; Guan, A.; Bathe, M.; Yin, P. *Science* **2014**, *346*, 717.
(27) Liu, W. Y.; Zhong, H.; Wang, R. S.; Seeman, N. C. *Angew. Chem., Int. Ed.* **2011**, *50*, 264.
(28) Fu, Y. M.; Zeng, D. D.; Chao, J.; Jin, Y. Q.; Zhang, Z.; Liu, H. J.; Li, D.; Ma, H. W.; Huang, Q.; Gothelf, K. V.; Fan, C. H. *J. Am. Chem. Soc.* **2013**, *135*, 696.
(29) Rajendran, A.; Endo, M.; Hidaka, K.; Sugiyama, H. *Chem. Commun.* **2013**, *49*, 686.
(30) Zhao, Z.; Liu, Y.; Yan, H. *Nano Lett.* **2011**, *11*, 2997.
(31) Iinuma, R.; Ke, Y. G.; Jungmann, R.; Schlichthaerle, T.; Woehrstein, J. B.; Yin, P. *Science* **2014**, *344*, 65.
(32) Woo, S.; Rothemund, P. W. K. *Nat. Chem.* **2011**, *3*, 620.
(33) Aghebat Rafat, A.; Pirzer, T.; Scheible, M. B.; Kostina, A.; Simmel, F. C. *Angew. Chem., Int. Ed.* **2014**, *53*, 7665.
(34) Woo, S.; Rothemund, P. W. K. *Nat. Commun.* **2014**, *5*, 4889.
(35) Kocabey, S.; Kempter, S.; List, J.; Xing, Y. Z.; Bae, W.; Schiffels, D.; Shih, W. M.; Simmel, F. C.; Liedl, T. *ACS Nano* **2015**, *9*, 3530.
(36) Suzuki, Y.; Endo, M.; Sugiyama, H. *Nat. Commun.* **2015**, *6*, 8052.
(37) Mitchell, J. C.; Harris, J. R.; Malo, J.; Bath, J.; Turberfield, A. J. *J. Am. Chem. Soc.* **2004**, *126*, 16342.
(38) Rothemund, P. W. K.; Ekani-Nkodo, A.; Papadakis, N.; Kumar, A.; Fygenson, D. K.; Winfree, E. *J. Am. Chem. Soc.* **2004**, *126*, 16344.

(39) Ke, Y. G.; Liu, Y.; Zhang, J. P.; Yan, H. *J. Am. Chem. Soc.* **2006**, *128*, 4414.

(40) Liu, H. P.; Chen, Y.; He, Y.; Ribbe, A. E.; Mao, C. D. *Angew. Chem., Int. Ed.* **2006**, *45*, 1942.

(41) Kuzuya, A.; Wang, R. S.; Sha, R. J.; Seeman, N. C. *Nano Lett.* **2007**, *7*, 1757.

(42) Yin, P.; Hariadi, R. F.; Sahu, S.; Choi, H. M. T.; Park, S. H.; LaBean, T. H.; Reif, J. H. *Science* **2008**, *321*, 824.

(43) Sharma, J.; Chhabra, R.; Cheng, A.; Brownell, J.; Liu, Y.; Yan, H. *Science* **2009**, *323*, 112.

(44) Mao, C. D.; Sun, W. Q.; Seeman, N. C. *J. Am. Chem. Soc.* **1999**, *121*, 5437.

(45) He, Y.; Chen, Y.; Liu, H. P.; Ribbe, A. E.; Mao, C. D. *J. Am. Chem. Soc.* **2005**, *127*, 12202.

(46) He, Y.; Tian, Y.; Chen, Y.; Deng, Z. X.; Ribbe, A. E.; Mao, C. D. *Angew. Chem., Int. Ed.* **2005**, *44*, 6694.

(47) Liu, H. P.; He, Y.; Ribbe, A. E.; Mao, C. D. *Biomacromolecules* **2005**, *6*, 2943.

(48) Liu, Y.; Ke, Y. G.; Yan, H. *J. Am. Chem. Soc.* **2005**, *127*, 17140.

(49) He, Y.; Tian, Y.; Ribbe, A. E.; Mao, C. D. *J. Am. Chem. Soc.* **2006**, *128*, 15978.

(50) Park, S. H.; Pistol, C.; Ahn, S. J.; Reif, J. H.; Lebeck, A. R.; Dwyer, C.; LaBean, T. H. *Angew. Chem., Int. Ed.* **2006**, *45*, 735.

(51) Castro, C. E.; Kilchherr, F.; Kim, D. N.; Shiao, E. L.; Wauer, T.; Wortmann, P.; Bathe, M.; Dietz, H. *Nat. Methods* **2011**, *8*, 221.

(52) Kim, D. N.; Kilchherr, F.; Dietz, H.; Bathe, M. *Nucleic Acids Res.* **2012**, *40*, 2862.

(53) Pan, K. Y.; Kim, D. N.; Zhang, F.; Adendorff, M. R.; Yan, H.; Bathe, M. *Nat. Commun.* **2014**, *5*, 5578.

(54) Fan, J. A.; Wu, C.; Bao, K.; Bao, J.; Bardhan, R.; Halas, N. J.; Manoharan, V. N.; Nordlander, P.; Shvets, G.; Capasso, F. *Science* **2010**, *328*, 1135.

(55) Lee, S. *Opt. Express* **2015**, *23*, 28170.

(56) Park, D. J.; Zhang, C.; Ku, J. C.; Zhou, Y.; Schatz, G. C.; Mirkin, C. A. *Proc. Natl. Acad. Sci. U. S. A.* **2015**, *112*, 977.

(57) Ross, M. B.; Ku, J. C.; Vaccarezza, V. M.; Schatz, G. C.; Mirkin, C. A. *Nat. Nanotechnol.* **2015**, *10*, 453.

(58) Sainidou, R.; Garcia de Abajo, F. J. *Opt. Express* **2008**, *16*, 4499.

(59) Shafiei, F.; Monticone, F.; Le, K. Q.; Liu, X. X.; Hartsfield, T.; Alu, A.; Li, X. Q. *Nat. Nanotechnol.* **2013**, *8*, 95.

(60) Tian, Y.; Wang, T.; Liu, W. Y.; Xin, H. L.; Li, H. L.; Ke, Y. G.; Shih, W. M.; Gang, O. *Nat. Nanotechnol.* **2015**, *10*, 637.

(61) Young, K. L.; Ross, M. B.; Blaber, M. G.; Rycenga, M.; Jones, M. R.; Zhang, C.; Senesi, A. J.; Lee, B.; Schatz, G. C.; Mirkin, C. A. *Adv. Mater.* **2014**, *26*, 653.

(62) Roller, E.; Khorashad, L. K.; Fedoruk, M.; Schreiber, R.; Govorov, A. O.; Liedl, T. *Nano Lett.* **2015**, *15*, 1368.

(63) Urban, M. J.; Dutta, P. K.; Wang, P. F.; Duan, X. Y.; Shen, X. B.; Ding, B. Q.; Ke, Y. G.; Liu, N. *J. Am. Chem. Soc.* **2016**, *138*, 5495.

(64) Sheikholeslami, S. N.; Alaeian, H.; Koh, A. L.; Dionne, J. A. *Nano Lett.* **2013**, *13*, 4137.

(65) Urzhumov, Y. A.; Shvets, G.; Fan, J.; Capasso, F.; Brandl, D.; Nordlander, P. *Opt. Express* **2007**, *15*, 14129.

(66) Monti, A.; Bilotti, F.; Toscano, A. *Opt. Lett.* **2011**, *36*, 4479.